Polarization microscopy with stellated gold nanoparticles for robust, *in-situ* monitoring of biomolecules

Jesse Aaron[1], Elder de la Rosa[2†], Kort Travis[3], Nathan Harrison[3], Justin Burt[2], Miguel José-Yacamán[2] and Konstantin Sokolov[1,4]*

[1]*Dept. Biomedical Engineering, University of Texas at Austin, Austin TX 78712*
[2]*Dept. Chemical Engineering, University of Texas at Austin, Austin TX 78712*
[3]*Dept. Physics, University of Texas at Austin, Austin TX 78712*
[4]*Depts. Biomedical Engineering and Imaging Physics, U.T. M.D. Anderson Cancer Center, Houston TX 77030*
[†] *On sabbatical from Centro de Investigaciones en Óptica (CIO), León, Gto. 37160, México*
To whom correspondence may be addressed. Phone: (512) 471-7440. Email: kostia@mail.utexas.edu

Abstract: Advances in plasmonic nanoparticle synthesis afford new opportunities for biosensing applications. Here, we apply a combination of a new type of plasmonic nanomaterial – stellated nanoparticles, and polarization-sensitive darkfield microscopy for detecting molecular assemblies and tracking of individual epidermal growth factor receptors within single live cells with high signal-to-background ratio. Depolarization of linear polarized light by stellated nanoparticles is over 15-fold more efficient than similarly-sized spheroidal nanoparticles. This efficient light depolarization allows robust detection of molecules labeled with stellated nanoparticles in cross-polarized imaging where the intrinsic light scattering from cells is significantly reduced. The imaging can be carried out with single molecule sensitivity for essentially unlimited time with no signal degradation.

OCIS codes: (170.3880) Medical and biological imaging; (250.5403) Plasmonics; (260.5430) Polarization; (170.1530) Cell analysis

References and links

1. D. S. Lidke, P. Nagy, R. Heintzmann, D. J. Arndt-Jovin, J. N. Post, H. E. Grecco, E. A. Jares-Erijman, and T. M. Jovin, "Quantum dot ligands provide new insights into erbB/HER receptor-mediated signal transduction," Nat. Biotechnol. **22**, 198-203 (2004).
2. M. Lakadamyali, M. J. Rust, H. P. Babcock, and X. Zhuang, "Visualizing infection of individual influenza viruses," Proc. Nat. Acad. Sci. **100**, 9280-9285 (2003).
3. L. Cai, N. Friedman, and X. S. Xie, "Stochastic protein expression in individual cells at the single molecule level," Nat. **440**, 358-362 (2006).
4. W. C. Chan, and S. Nie, "Quantum dot bioconjugates for ultrasensitive nonisotopic detection," Science **281**, 2016-2018. (1998).
5. X. Gao, W. C. W. Chan, and S. Nie, "Quantum-dot nanocrystals for ultrasensitive biological labeling and multicolor optical encoding," J. Biomed. Opt. **7**, 532-537 (2002).
6. C. Boozer, G. Kim, S. Cong, H. Guan, and T. Londergan, "Looking towards label-free biomolecular interaction analysis in a highthroughput format: a review of new surface plasmon resonance technologies," Curr. Opin. Biotechnol. **17**, 400-405 (2006).
7. N. Calander, "Molecular detection and analysis by using surface plasmon resonances," Curr. Anal. Chem. **2**, 203-211 (2006).
8. P. Alivisatos, "The use of nanocrystals in biological detection," Nat. Biotechnol. **22**, 47-52 (2004).
9. C. Soennichsen, B. M. Reinhard, J. Liphardt, and A. P. Alivisatos, "A molecular ruler based on plasmon coupling of single gold and silver nanoparticles," Nat. Biotechnol. **23**, 741-745 (2005).
10. K. Sokolov, M. Follen, J. Aaron, I. Pavlova, A. Malpica, R. Lotan, and R. Richards-Kortum, "Real-time vital optical imaging of precancer using anti-epidermal growth factor receptor antibodies conjugated to gold nanoparticles," Cancer Res. **63**, 1999-2004 (2003).

11. J. Aaron, N. Nitin, K. Travis, S. Kumar, T. Collier, S. Y. Park, M. Jose-Yacaman, L. Coghlan, M. Follen, R. Richards-Kortum, and K. Sokolov, "Plasmon Resonance Coupling of Metal Nanoparticles for Molecular Imaging of Carcinogenesis In Vivo," J. Biomed. Opt. **12**, 034007 (2007).
12. I. H. El-Sayed, X. Huang, and M. A. El-Sayed, "Surface plasmon resonance scattering and absorption of anti-EGFR antibody conjugated gold nanoparticles in cancer diagnostics: Applications in oral cancer," Nano Lett. **5**, 829-834 (2005).
13. C. Loo, L. Hirsch, M.-H. Lee, E. Chang, J. West, N. Halas, and R. Drezek, "Gold nanoshell bioconjugates for molecular imaging in living cells," Opt. Lett. **30**, 1012-1014 (2005).
14. S. Mallidi, T. Larson, J. Aaron, K. Sokolov, and S. Emelianov, "Molecular specific optoacoustic imaging with plasmonic nanoparticles," Opt. Express **15**, 6583-6588 (2007).
15. T. A. Larson, J. Bankson, J. Aaron, and K. Sokolov, "Hybrid plasmonic magnetic nanoparticles as molecular specific agents for MRI/optical imaging and photothermal therapy of cancer cells," Nanotechnol. **18**, 325101 (2007).
16. L. R. Hirsch, R. J. Stafford, J. A. Bankson, S. R. Sershen, B. Rivera, R. E. Price, J. D. Hazle, N. J. Halas, and J. L. West, "Nanoshell-mediated near-infrared thermal therapy of tumors under magnetic resonance guidance," Proc. Nat. Acad. Sci. **100**, 13549-13554 (2003).
17. C. M. Pitsillides, E. K. Joe, X. Wei, R. R. Anderson, and C. P. Lin, "Selective cell targeting with light-absorbing microparticles and nanoparticles," Biophys. J. **84**, 4023-4032 (2003).
18. C. Loo, A. Lowery, N. Halas, J. West, and R. Drezek, "Immunotargeted Nanoshells for Integrated Cancer Imaging and Therapy," Nano Lett. **5**, 709-711 (2005).
19. R. Shukla, V. Bansal, M. Chaudhary, A. Basu, R. R. Bhonde, and M. Sastry, "Biocompatibility of Gold Nanoparticles and Their Endocytotic Fate Inside the Cellular Compartment: A Microscopic Overview," Langmuir **21**, 10644-10654 (2005).
20. S. Schultz, D. R. Smith, J. J. Mock, and D. A. Schultz, "Single-target molecule detection with nonbleaching multicolor optical immunolabels," Proc. Nat. Acad. Sci. **97**, 996-1001 (2000).
21. C. S. Thaxton, and C. A. Mirkin, "DNA-gold-nanoparticle conjugates," Nanobiotechnol., 288-307 (2004).
22. C. Oliver, "Conjugation of colloidal gold to proteins," Meth. Mol. Bio. **115**, 331-334 (1999).
23. S. Kumar, N. Harrison, R. Richards-Kortum, and K. Sokolov, "Plasmonic Nanosensors for Imaging Intracellular Biomarkers in Live Cells," Nano Lett. **7**, 1338-1343 (2007).
24. S. J. Oldenburg, R. D. Averitt, S. L. Westcott, and N. J. Halas, "Nanoengineering of optical resonances," Chem. Phys. Lett. **288**, 243-247 (1998).
25. A. V. Alekseeva, V. A. Bogatyrev, B. N. Khlebtsov, A. G. Mel'nikov, L. A. Dykman, and N. G. Khlebtsov, "Gold nanorods: Synthesis and optical properties," Colloid J. **68**, 661-678 (2006).
26. M. B. Mohamed, V. Volkov, S. Link, and M. A. El-Sayed, "The `lightning' gold nanorods: fluorescence enhancement of over a million compared to the gold metal," Chem. Phys. Lett. **317**, 517-523 (2000).
27. N. J. Durr, T. Larson, D. K. Smith, B. A. Korgel, K. Sokolov, and A. Ben-Yakar, "Two-Photon Luminescence Imaging of Cancer Cells Using Molecularly Targeted Gold Nanorods," Nano Lett. **7**, 941-945 (2007).
28. M. L. Sandrock, C. D. Pibel, F. M. Geiger, and C. A. Foss, Jr., "Synthesis and Second-Harmonic Generation Studies of Noncentrosymmetric Gold Nanostructures," J. Phys. Chem. B **103**, 2668-2673 (1999).
29. H. Wang, T. B. Huff, D. A. Zweifel, W. He, P. S. Low, A. Wei, and J.-X. Cheng, "In vitro and in vivo two-photon luminescence imaging of single gold nanorods," Proc. Nat. Acad. Sci. **102**, 15752-15756 (2005).
30. J. Chen, F. Saeki, B. J. Wiley, H. Cang, M. J. Cobb, Z.-Y. Li, L. Au, H. Zhang, M. B. Kimmey, X. Li, and Y. Xia, "Gold Nanocages: Bioconjugation and Their Potential Use as Optical Imaging Contrast Agents," Nano Lett. **5**, 5 (2005).
31. Y. Lu, G. L. Liu, J. Kim, Y. X. Mejia, and L. P. Lee, "Nanophotonic Crescent Moon Structures with Sharp Edge for Ultrasensitive Biomolecular Detection by Local Electromagnetic Field Enhancement Effect," Nano Lett. **5**, 119-124 (2005).
32. J. Aizpurua, P. Hanarp, D. S. Sutherland, M. Käll, G. W. Bryant, and F. J. García de Abajo, "Optical Properties of Gold Nanorings," Phys. Rev. Lett. **90**, 057401 (2003).
33. F. Hao, C. L. Nehl, J. H. Hafner, and P. Nordlander, "Plasmon Resonances of a Gold Nanostar," Nano Lett. **7**, 729-732 (2007).
34. C. L. Nehl, H. Liao, and J. H. Hafner, "Optical Properties of Star-Shaped Gold Nanoparticles," Nano Lett. **6**, 683-688 (2006).
35. J. L. Burt, J. L. Elechiguerra, J. Reyes-Gasga, J. Martin Montejano-Carrizales, and M. Jose-Yacaman, "Beyond Archimedean solids: Star polyhedral gold nanocrystals," J. Cryst. Growth **285**, 681-691 (2005).
36. C. Soennichsen, and A. P. Alivisatos, "Gold Nanorods as Novel Nonbleaching Plasmon-Based Orientation Sensors for Polarized Single-Particle Microscopy," Nano Letters **5**, 301-304 (2005).
37. J. P. Kottmann, O. J. F. Martin, D. R. Smith, and S. Schultz, "Field polarization and polarization charge distributions in plasmon resonant nanoparticles," New J. Phys. **2**, Article No. 27 (2000).
38. J. J. Mock, S. J. Oldenburg, D. R. Smith, D. A. Schultz, and S. Schultz, "Composite Plasmon Resonant Nanowires," Nano Lett. **2**, 465-469 (2002).
39. M. L. Sandrock, and C. A. Foss, Jr., "Synthesis and Linear Optical Properties of Nanoscopic Gold Particle Pair Structures," J. Phys. Chem. B **103**, 11398-11406 (1999).
40. W. Rechberger, A. Hohenau, A. Leitner, J. R. Krenn, B. Lamprecht, and F. R. Aussenegg, "Optical properties of two interacting gold nanoparticles," Opt. Commun. **220**, 137-141 (2003).
41. L. Nieman, A. Myakov, J. Aaron, and K. Sokolov, "Optical sectioning using a fiber probe with an angled illumination-collection geometry: evaluation in engineered tissue phantoms," Appl. Opt. **43**, 1308-1319 (2004).

42. S. L. Jacques, J. R. Roman, and K. Lee, "Imaging superficial tissues with polarized light," Laser. Surg. Med. **26**, 119-129. (2000).
43. C. J. Barnes, and R. Kumar, "Biology of the epidermal growth factor receptor family," Cancer Treat. Res. **119**, 1-13 (2004).
44. K. R. Brown, and M. J. Natan, "Hydroxylamine Seeding of Colloidal Au Nanoparticles in Solution and on Surfaces," Langmuir **14**, 726-728 (1998).
45. G. Frens, "Controlled nucleation for the regulation of the particle size in monodisperse gold suspensions," Nat. Phys. Sci. **241**, 20-22 (1973).
46. J. S. Aaron, J. Oh, T. A. Larson, S. Kumar, T. E. Milner, and K. V. Sokolov, "Increased optical contrast in imaging of epidermal growth factor receptor using magnetically actuated hybrid gold/iron oxide nanoparticles," Opt. Express **14**, 12930-12943 (2006).
47. J. M. Lerner, "Imaging Spectrometer Fundamentals for Researchers in the Biosciences—A Tutorial," Cytomet. A **69A**, 712-734 (2006).
48. M. I. Mishchenko, L. D. Travis, and D. W. Mackowski, "Capabilities andLimitations of a Current FORTRAN Implementation of the T-Matrix Method for Randomly Oriented, Rotationally Symmetric Scatterers.," J. Quant. Spectrosc. Radiat. Transfer **60**, 309-324 (1998).
49. M. I. Mishchenko, L. D. Travis, and D. W. Mackowski, "T-matrix computations of light scattering by nonspherical particles: a review," J. Quant. Spectrosc. Radiat. Transfer **55**, 535-575 (1996).
50. D. W. Mackowski., "Analysis of Radiative Scattering for Multiple Sphere Configurations," Proc. R. Soc. Lond. **433**, 599-614 (1991).
51. D. W. Mackowski, "Calculation of total cross sections of multiplesphere clusters," J. Opt. Soc. Am. **11**, 2851-2861 (1994).
52. D. W. Mackowski, and M. I. Mishchenko, "Calculation of the T-matrix and the scattering matrix for ensembles of spheres," J. Opt. Soc. Am. A **13**, 2266-2278 (1996).
53. B. Stout, J.-C. Auger, and J. Lafait, "A transfer matrix approach to local field calculations in multiple-scattering problems.," Journal of Modern Optics **49**, 2129-2152 (2002).
54. B. T. Draine, and P. J. Flatau, "Discrete-dipole approximation for scattering calculations," J. Opt. Soc. Am. A **11**, 1491- (1994).
55. M. A. Yurkin, V. P. Maltsev, and A. G. Hoekstra, "The discrete dipole approximation for simulation of light scattering by particles much larger than the wavelength.," J. Quant. Spectrosc. Radiat. Transfer **106**, 546-557 (2007).
56. P. B. Johnson, and R. W. Christy, "Optical constants of the noble metals," Phys. Rev. B **6**, 4370-4379 (1972).
57. U. Kreibig, "Properties of Small Particles in Insulating Matrices," in *Contribution of Clusters Physics to Material Science and Technology From Isolated Clusters to Aggregated Materials*, J. Davenas, and P. M. Rabette, eds. (Klewer Academic Publishers, New York, NY, 1986), pp. 373-423.
58. P. Schiebener, J. Straub, J. M. H. L. Sengers, and J. S. Gallagher, "Release on the Refractive Index of Ordinary Water Substance as a function of Wavelength, Temperature and Pressure.," in *Technical Report* (The International Association for the Properties of Water and Steam (IAPWS), 1997).
59. R. N. Fabricant, J. E. D. Larco, and G. J. Todaro, "Nerve Growth Factor Receptors on Human Melanoma Cells in Culture," Proc. Nat. Acad. Sci. **74**, 565-569 (1977).
60. M. M. Wrann, and C. F. Fox, "Identification of epidermal growth factor receptors in a hyperproducing human epidermoid carcinoma cell line," J. Bio. Chem. **254**, 8083-8086 (1979).
61. A. Vieira, C. Lamaze, and S. L. Schmid, "Control of EGF receptor signaling by clathrin-mediated endocytosis," Science **274**, 2086-2089 (1996).
62. G. Carpenter, "Receptors for Epidermal Growth Factor and Other Polypeptide Mitogens," Annu. Rev. Biochem. **56**, 881-914 (1987).
63. P. Burke, K. Schooler, and H. S. Wiley, "Regulation of epidermal growth factor receptor signaling by endocytosis and intracellular trafficking," Mol. Bio. Cell **12**, 1897-1910 (2001).
64. T. Basche, S. Nie, and J. M. Fernandez, "Single molecules," Proc. Nat. Acad. Sci. **98**, 10527-10528 (2001).
65. T. Wilson, and B. R. Masters, "Confocal Microscopy," Appl. Opt. **33**, 565 (1994).
66. R. Brock, M. A. Hink, and T. M. Jovin, "Fluorescence Correlation Microscopy of Cells in the Presence of Autofluorescence," Biophys. J. **75**, 2547-2557 (1998).
67. D. Axelrod, "Total Internal Reflection Fluorescence Microscopy in Cell Biology," Traffic **2**, 764-774 (2001).
68. T. A. Byassee, W. C. W. Chan, and S. Nie, "Probing Single Molecules in Single Living Cells," Anal. Chem. **72**, 5606-5611 (2000).
69. L. Cognet, C. Tardin, D. Boyer, D. Choquet, P. Tamarat, and B. Lounis, "Single metallic nanoparticle imaging for protein detection in cells," Proc. Nat. Acad. Sci. **100**, 11350-11355 (2003).
70. G. I. Mashanov, D. Tacon, A. E. Knight, M. Peckham, and J. E. Molloy, "Visualizing single molecules inside living cells using total internal reflection fluorescence microscopy," Methods **29**, 142-152 (2003).
71. V. Sankaran, M. J. Everett, D. J. Maitland, and J. T. Walsh, "Comparison of polarized-light propagation in biological tissue and phantoms," Opt. Lett. **25**, 1044-1046 (1999).
72. R. S. Gurjar, V. Backman, L. T. Perelman, I. Georgakoudi, K. Badizadegan, I. Itzkan, R. R. Dasari, and M. S. Feld, "Imaging human epithelial properties with polarized light-scattering spectroscopy," Nat. Med. 7, 1245-1248 (2001).
73. V. Backman, R. Gurjar, K. Badizadegan, I. Itzkan, R. R. Dasari, L. T. Perelman, and M. S. Feld, "Polarized light scattering spectroscopy for quantitative measurement of epithelial cellular structures in situ," IEEE J. Sel. Top. Quantum Electron. **5**, 1019-1026 (1999).

74. K. Sokolov, R. Drezek, K. Gossage, and R. Richards-Kortum, "Reflectance spectroscopy with polarized light: is it sensitive to cellular and nuclear morphology?," Opt. Express **15**, 302-317 (1999).
75. P. M. F. Nielsen, F. N. Reinholz, and P. G. Charette, "Polarization-sensitive scanned fiber confocal microscope," Opt. Engr. **35**, 3084-3091 (1996).
76. J. F. de Boer, T. E. Milner, M. J. C. van Gemert, and J. S. Nelson, "Two-dimensional birefringence imaging in biological tissue by polarization-sensitive optical coherence tomography," Opt. Lett. **22**, 934 (1997).
77. S. Kumar, J.S. Aaron, K.V. Sokolov, " Directional conjugation of antibodies to nanoparticles for Ssynthesis of multiplexed optical contrast agents with both delivery and targeting moieties" Nat. Protocols (2008) (in press).

1. Introduction

Development of new probes for the detection of molecular events in single living cells can lead to a better understanding of challenging clinical problems such as cancer. It is highly desirable that these probes facilitate robust detection of single molecules and single molecular events. Fluorescent dyes and genetically-encoded fluorescent proteins (e.g., green fluorescent protein, GFP) are very useful probes for molecular imaging; however, they do not routinely provide enough signal for single molecule detection in live cells. Recently, elegant work has been published on activation of single epidermal growth factor receptors [1] and single viral trafficking [2] using quantum dots (qdots), as well as stochastic protein expression in yeast and bacteria using organic dyes [3]. Although qdots can provide single molecule sensitivity, they also have certain drawbacks including blinking effects and susceptibility to photobleaching over time [3, 4]. In addition, qdots are also prepared using highly toxic semiconductor materials, making development of stable biocompatible coating chemistry essential [5].

Recently, localized surface plasmon resonance phenomena have been utilized in nanometer-sized gold particles for a multitude of biosensing applications with excellent sensitivity, down to single molecular binding events [6-9]. The large optical scattering cross-section of plasmonic nanoparticles makes them appealing as molecular specific labels for reflectance-based imaging [10-13], and their strong absorption properties facilitate applications to photoacoustic imaging [14] and to combined imaging and photothermal therapy approaches [15-18]. The attractiveness of this technology for biosensing applications is also due to several other factors, including chemical inertness[19]; stable signal intensity due to lack of photobleaching or blinking effects [20]; convenient surface functionalization strategies [21, 22]-[23]; and strong sensitivity to other resonant scatterers in the near-field, (termed plasmon coupling) that can give nano-scale information about interactions and distribution of biomolecules [9, 11].

To complement these inherent properties, exciting advances in nanomaterial engineering have produced a large array of particle geometries that have created new opportunities for biological applications of plasmonics. Such novel shapes include dielectric core-metal shell nanoparticles (nanoshells), which can be spectrally tuned over a wide optical range[24], metal nanorods [25]-[26] that can be used as sources of second harmonic generation and two-photon luminescence [27-29], nanocages [30], nanocrescents and rings [31, 32], as well as the stellated nanoparticles [33-35] used in the present work among many other examples.

A feature of plasmonic nanoparticles that has not been widely explored in a biosensing context is the effect of nanoparticle plasmon resonance on light polarization. Single nanoparticles or their assemblies containing geometrical asymmetry will cause light depolarization, depending on the relative orientation of nanoparticles and the incident light's polarization. This phenomenon was well characterized in the case of nanorods[36-38], and lithographically prepared pairs of ellipsoidal particles [39, 40]. Recently, star-shaped nanoparticles were also shown to have interesting and complex light polarization dependent properties [33, 34], due to their inherent asymmetry. Although not fully characterized, the stellated geometry results in strong overall light depolarization in the red and near infrared (NIR) spectral region from single particles. Additionally, these type of nanoparticles can be synthesized without the need for complex seeding or surfactant-based methods [35] that are used in preparation of other specially-shaped particles, such as nanorods.

Here we demonstrate that the optical properties of stellated gold nanoparticles provide an opportunity to apply this nanomaterial as biomolecular-specific probes in combination with polarization-sensitive imaging. It is well known that live cells do not significantly alter light polarization state [41, 42], particularly in the NIR region. Therefore, the use of polarization microscopy in combination with asymmetric plasmonic nanoparticles can provide a sensitive molecular imaging approach by drastically reducing the endogenous scattering background signal when used to label cells or other biological tissues.

We compared spherical and stellated nanoparticles of approximately the same size as molecular-specific contrast agents for polarization microscopy of epidermal growth factor receptor (EGFR) expression – an important indicator of cancerous or pre-cancerous growth [43] – in live cells. We showed that while isolated spherical particles do not appreciably alter linear polarized light, EGFR mediated assemblies of these particles on the cell surface result in more prominent changes in light polarization. In contrast, similarly-sized stellated gold nanoparticles can more efficiently depolarize light in both isolated and aggregated cases. We demonstrate that molecular targeted spherical and stellated gold nanoparticles can be used for sensitive detection of cancer cells using a simple detection scheme with a linear-polarized excitation and a cross-polarized analyzer. Furthermore, the unique properties of stellated nanoparticles allow the monitoring of single EGFR trafficking events within live cells with high signal to noise ratio for an essentially unlimited period of time.

2. Materials and methods

2.1. Nanoparticle synthesis and characterization

Stellated gold nanoparticles were synthesized by a simple procedure based on the colloidal reduction of chloroauric acid ($HAuCl_4$) in a homogeneous solution of ascorbic acid (H_2A) in water at 0 °C. In a typical experiment, 1.4 g of H_2A was dissolved in 40 mL of deionized water. Then, 0.5 mL of 0.1M $HAuCl_4$ solution was added rapidly under vigorous stirring. The solution immediately acquires a blue color that after few seconds becomes an opaque dark brown color. The solution was kept under strong stirring for 15 minutes.

Highly monodisperse spherical gold nanoparticles were synthesized using the protocol reported by Brown and Natan [44]. In this procedure, *ca.* 15nm gold nanoparticle "seeds", synthesized by a citrate reduction method [45], are combined at room temperature with an aqueous solution of 0.01% $HAuCl_4$ and 40mM NH_2OH. The latter component catalyzes gold ion reduction at the seed surface. This method generally produces a higher monodispersity of larger particles than the citrate reduction method alone.

Analysis of TEM images (not shown), acquired with a Philips EM 208 TEM, revealed that the spherical nanoparticles have an average diameter of approximately 65±5nm, while the stellated particles were *ca.* 81±21nm in diameter. Clearly, there is more shape heterogeneity with the stellated particles than with the spheres. It was determined from electron diffraction spectra that stellated nanoparticles are composed of a small number of symmetrically-aligned, monocrystalline domains (data not shown). Further, TEM imaging reveals that 70% of the nanoparticles are stellated in nature, while the remaining 30% are composed of rounded crystals with non-uniform distribution of stellations on the surface. A detailed analysis of the crystalline structure was reported previously [35].

Particles were also characterized using a Zeiss Supra 40 VP Scanning Electron Microscope (SEM). Indium-tin oxide (ITO) coated glass coverslips (SPI Supplies) were first cleaned via plasma etching (Oxford Instruments Plasma Lab 80+). Small marks were placed on the coverslips using a laboratory marker (to aid in co-registering optical and electron microscopy images), and the surface was then exposed to a small volume of solution containing either spherical or stellated nanoparticles for 10 minutes at room temperature. Coverslips were then extensively washed in de-ionized H_2O.

2.2 Bioconjugation of nanoparticles with anti-EGFR antibodies and cell culturing

We conjugated both types of nanoparticles to anti-EGFR monoclonal antibodies using a previously described protocol [23, 46].   Briefly, anti-EGFR monoclonal antibodies (Sigma, clone 29.1.1) at a concentration of 1 mg/mL were exposed to 10mM $NaIO_4$ in 40mM HEPES for 30 minutes at room temperature. During this step, the glycosylated Fc portion of the antibody is oxidized. Subsequently, the oxidized antibodies were mixed with an excess of a hetero-bifunctional polyethylene glycol (PEG) linker containing a hydrazide and thiol moiety on either end (Sensopath Technologies, SPT-0014B) for 30 minutes at room temperature. In this step, the hydrazide moiety on the linker binds covalently to the non-targeting Fc portion of the antibody, while the thiol group remains available for binding to gold surfaces. The antibody-linker complexes were separated from unbound linker via centrifugal filtration (Millipore, 100kDa MWCO) and resuspended at 1mg/mL antibody concentration in 1x PBS.

Subsequently, anti-EGFR antibodies were attached to gold nanoparticles by mixing a solution of 5μg/mL antibody-linker in 40mM HEPES (pH 7.4) with an equal volume of a nanoparticle solution for 20 minutes, followed by addition of 10^{-5} M of monofunctional mPEG-thiol (5kD, Nektar) in order to passivate any remaining exposed particle surface. Conjugates were centrifuged at *ca.* 1700 x rcf for 10-15 minutes and resuspended in 1x PBS containing 1 mM $CaCl_2$, 1 mM $MgCl_2$, 0.2% BSA and 5 mM D-(+)-glucose (Sigma) to maintain cell viability during labeling experiments. Suspensions of nanoparticle-antibody conjugates were centrifuged at *ca.* 100x RCF for 3 minutes just prior to cell labeling experiments in order to remove aggregates that can potentially form during particle storage. All cells used for molecular specific imaging were cultured in Dulbecco's Modified Eagle Medium (DMEM) supplemented with 5% FBS at 37°C and 5% CO_2 environment.

2.3 Darkfield microscopy and Hyperspectral imaging

The optical scattering properties of both types of nanoparticles were assessed using a Leica DM6000 microscope in transmission darkfield mode. Images of isolated particles on ITO glass coverslips, as well as images of single particle trafficking in live cells were acquired using a 40x 0.75NA biological objective and quartz halogen light source coupled to a 1.2-1.4NA oil immersion darkfield condenser. Images of labeled cells were acquired using the same optical set, except a 20x 0.5NA brightfield/darkfield objective was used. For experiments with isolated particles, registration marks were used to align the field of view to match that seen in SEM images of the same particles.

In all optical imaging experiments, a polarizer was attached to the microscope condenser to provide linear-polarized illumination light, and an analyzing polarizer was placed in the detection path with its axis either parallel or perpendicular to the incident polarization. Images were acquired using a Q-Imaging 12-bit Retiga EXi CCD camera with an LCD filter attachment for RGB imaging. Camera exposure times and gain settings were adjusted for each sample and imaging mode to maximize signal to noise ratio. The overall sensitivity differences between each acquisition condition were determined by imaging a spectral calibration standard (Spectralon, LabSphere, Inc.).   Scattering spectra from individual nanoparticles and from cells were measured using a stage-scanning, prism dispersion based hyperspectral microscopy system (Lightform Inc., PARISS®) [47], which was coupled to the darkfield Leica microscope. The hyperspectral system is capable of acquiring a complete scattering spectrum from individual particles, with 0.6μm spatial resolution at 40x magnification and 1nm spectral resolution. All hyperspectral data were analyzed in Matlab.

2.4 Electrodynamic simulations

We carried out electrodynamic simulations to theoretically assess the depolarization capability of each nanoparticle type, and to determine to what extent plasmon coupling plays a role in the observed effects. The T-matrix technique [48, 49], its extension to aggregates [50-53], and the Discrete Dipole Approximation (DDA) were deemed to be the most appropriate methods [54] to accurately model the optical scattering from plasmon resonant nanoparticles and their

aggregates. The T-matrix technique is most suitable to model scattering from single particles with azimuthal symmetry (such as spheroidal particles), and from aggregates of such particles. In contrast, the DDA technique is well suited to the modeling of particles possessing complicated, non-symmetric shapes, such as stellated particles. The T-matrix code used in these studies is a new code implemented completely in C++, and is based primarily on the theoretical work discussed in [50-53]. The DDA code is available in the public domain [55], and has been supplemented with custom C++ utilities in order to allow computation for particles defined by any arbitrary closed-mesh surface. The specifics of the material permittivity function are particularly important when modeling plasmon resonant materials. For both simulation techniques, the permittivity function used for Au is based on the experimental data published in [56] with an additional size-dependent electron mean-free-path correction applied as detailed in [57]. While this correction is negligible for the particle sizes that were used in this study, we would like to emphasize that in general care must be taken with the material functions in order to ensure high-quality simulation results. The permittivity function used for H_2O is based on the formula published in [58].

3. Results and discussion

3.1 Light scattering properties of single nanoparticles

Figures 1A and B show four representative examples of high-resolution SEM images of individual spherical and stellated nanoparticles, respectively. Images indicate that spheroidal particles retain a relatively smooth particle surface and smaller average aspect ratio as compared to stellated nanoparticles. Also, 6-8 stellations per particle can be identified in Fig. 1(b). Figures 1(c) and (d) show a series of color darkfield images of spherical and stellated gold nanoparticles, respectively. The individually numbered particles seen in SEM images correspond to the matching numbered particles displayed in the optical images. For Figs. 1(c) and 1(d), an un-polarized darkfield image is shown at top. The middle images indicate darkfield illumination with horizontally polarized light, and detection of scattering with parallel polarization to the incident illumination. Bottom images in Figs. 1(c) and 1(d) were taken under darkfield illumination with cross-polarized (perpendicular) detection. It should be noted that for both particle types, the images with parallel and perpendicular orientation of polarizers were acquired using acquisition conditions with 2.5-fold and 15-fold enhanced sensitivity, respectively, relative to the images acquired without polarizers. This adjustment was used to optimize signal-to-noise ratio (SNR) as well as to compensate for light absorption by the polarizers and a dependence of light throughput in the microscope on polarization axis.

Comparison of SEM images (Figs. 1(a) and 1(b)) with the corresponding darkfield images (Figs. 1(c) and 1(d)) indicates that shape differences between the two particle types correlate with marked differences in their depolarization properties. The spherical particles scatter predominantly in the green to orange range (Fig. 1(c)) while stellated particles scatter primarily in the red optical region (Fig. 1(d)). Images of both particle populations with polarizer/analyzer in parallel configuration (Figs. 1(c) and 1(d), middle) are similar to images taken without polarizers (Figs. 1(c) and 1(d), top). However, imaging with cross-polarized configuration (Figs. 1(c) and 1(d), bottom) reveals drastic differences in how much light each particle type can depolarize. The ability of nanoparticles to depolarize light can be evaluated by computing the ratio of each particle's parallel and perpendicular signal. For the nearly spherical particles used, this value averages about 1%, but for stellated particles, the value increases dramatically to nearly 15%. There is one spherical particle in Fig. 1(c), bottom, that also displays noticeable light depolarization. SEM analysis (not shown) indicates that this particular particle is highly a-spherical (with an aspect ratio of nearly 1.2), that can explain its aberrant scattering behavior.
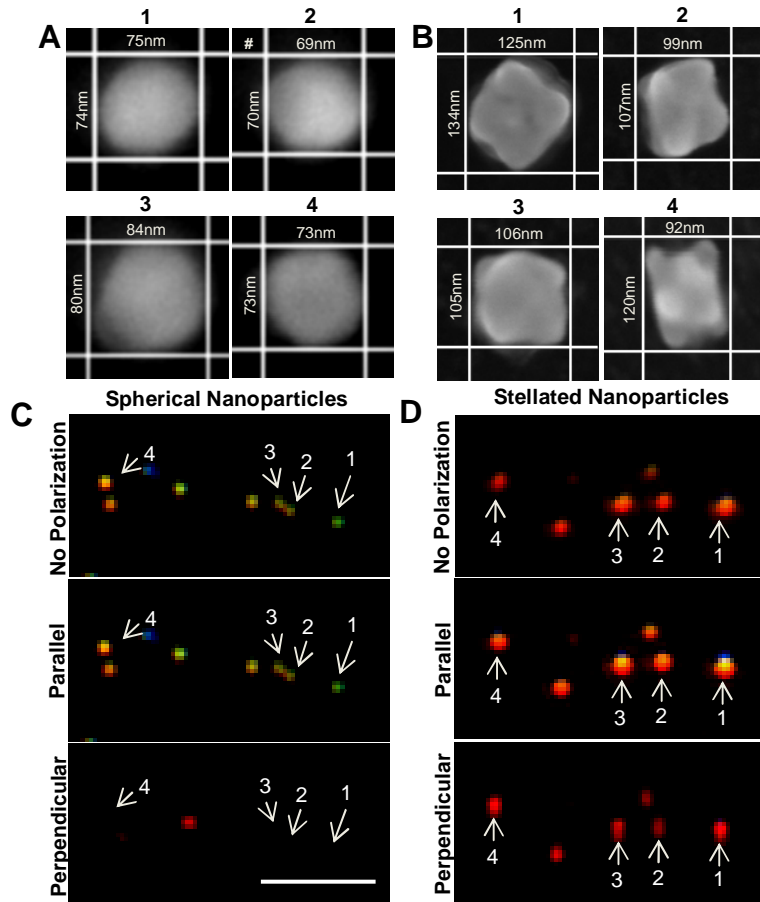
Fig. 1. Characterization of spherical and stellated gold nanoparticles. In (A) and (B), four representative SEM images (taken with Zeiss Supra 40 VP at 200K-400K magnification) are shown which reveal the shape differences between spherical and stellated nanoparticles, respectively. (C) and (D) show darkfield images of spherical and stellated particles, respectively, which were obtained under different illumination/collection conditions. Note that the numbered particles in the darkfield images correspond to numbered particles in the SEM images. Top images are acquired with unpolarized darkfield illumination. Middle images were taken with horizontally polarized illumination, and detection of scattered light with parallel orientation of the analyzing polarizer (parallel polarization). Bottom images show the scattering with polarization perpendicular relative to the illumination (perpendicular polarization). Note that most of spherical particles are not visible under perpendicular polarization. Images with parallel and perpendicular orientation of polarizer and analyzer were acquired using acquisition conditions with 2.5x and 15x enhanced sensitivity, respectively, relative to images without polarizers. Scale bar is 5μm.

Figure 2 shows representative scattering spectra of a spherical (blue curve) and a stellated (red curve) gold nanoparticle acquired using the hyperspectral imaging system. The spherical nanoparticle spectrum corresponds to particle number 4 indicated in Figs. 1(a) and 1(c), while the stellated nanoparticle spectrum corresponds to particle number 2 indicated in Figs. 1(b) and 1(d). Both spectra are normalized such that the peak scattering intensity is unity. Analysis of more than 100 particles of each type indicates that the average plasmon resonance wavelength of the green spherical particles is 548±16nm, while that of the stellated particles is 630±33nm. The variations of peak wavelength can be attributed to particle size/shape heterogeneity; thus it is apparent that the stellated nanoparticles have a much more diverse

shape/size distribution than that of the isolated spheres. This is consistent with SEM images and previously published TEM analysis [35].
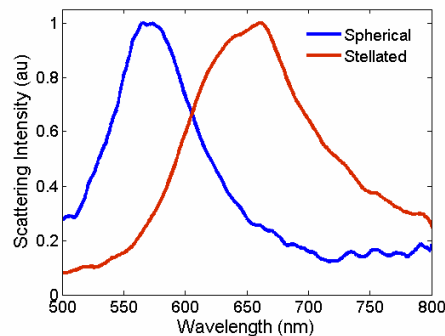

Fig. 2. Representative scattering spectra of individual spherical (blue) and stellated (red) nanoparticles obtained using the PARISS hyperspectral imaging system (Lightform, Inc.) coupled to the Leica DM6000. The blue spectrum corresponds to the spherical particle number 4 shown in (A) and the red spectrum corresponds to the stellated particle number 2 shown in (B). Analysis of the scattering spectra from N>100 particles of each type showed that the average peak wavelength for spheres is 548 ± 16 nm, and 630 ± 33 nm for stellated particles.

2.3. Electrodynamic simulations

We carried out simulations of scattering cross sections for three different cases. First, the polarization-sensitive scattering cross-section was calculated for a single 75nm spheroidal particle with an aspect ratio of 1.05 to approximate a real world, non-ideal geometry (note that a perfectly spherical particle does not produce any depolarization). Second, the scattering profile from an aggregate of 8 spherical particles, each with center-to-center separation of 1.15 times the particle diameter was simulated, to approximate the configuration of particles seen on the cell surface [11]. T-matrix simulations use a particle-centered maximum multipole order of 6. Finally, in order to simulate as closely as possible the observed stellated nanoparticle morphology, a stellated octahedron (a star-shape with 8 points) was used, with the stellations smoothed to match the real-world geometry. The aspect ratio of the stellated octahedron was adjusted to 1.3, which matches the SEM image of stellated particle number 2, shown in Fig. 1(b). DDA simulations used a cubic grid with 100 points along each edge. In each case, a particle or the aggregate was oriented with respect to the illumination polarization in order to produce maximum depolarization. Note that the simulation beam geometry is simplified significantly in comparison to the actual experimental dark field illumination geometry, which has a high incident beam angle, and implicitly averages over an angular range; these factors were not included in the simulation for reasons of computational tractability. Images of the particle/aggregate geometry are shown in Fig. 3(a), and were generated using POV-Ray, a freely available ray-tracing software package. In these images, the light propagation vector extends in the z-direction (into the page). Scattering cross sections with parallel and perpendicular polarizations relative to the incident polarization were calculated for illumination and collection in the z-direction, and are shown in Fig. 3(b).

The simulated spectra in Fig. 3(b), left, show the scattering profile of light with polarization parallel to the incident light, each normalized to a maximum of one. Simulated spheroidal and spherical particle aggregate spectra are consistent with previous measurements [10, 11]. Stellated nanoparticles and aggregated spheres show a red-shifted plasmon peak as compared to spherical particles. The peak position, however, depends heavily on the precise geometrical morphology of the stellated particle. Particles with differing peak numbers, more rounded or pointed points, and other modifications produce significantly different spectra. Figure 3(b), right, shows relative scattering cross sections with polarization perpendicular to the incident light. These theoretical spectra indicate the depolarization ability of each particle

type or aggregate relative to the parallel component which is normalized to one at its maximum (Fig. 3(b), left). Note that while a single spheroid particle only depolarizes up to 1% of the incoming light, an aggregate of 8 spherical particles will depolarize up to 7% of the incoming light. The single stellated particle of geometry illustrated in Fig. 3(a) (constructed to closely match the morphology of particle number 2 in Fig. 1(b)) depolarizes up to 15% of the illumination light. This value is consistent with analysis of the darkfield images in Figure 1D.
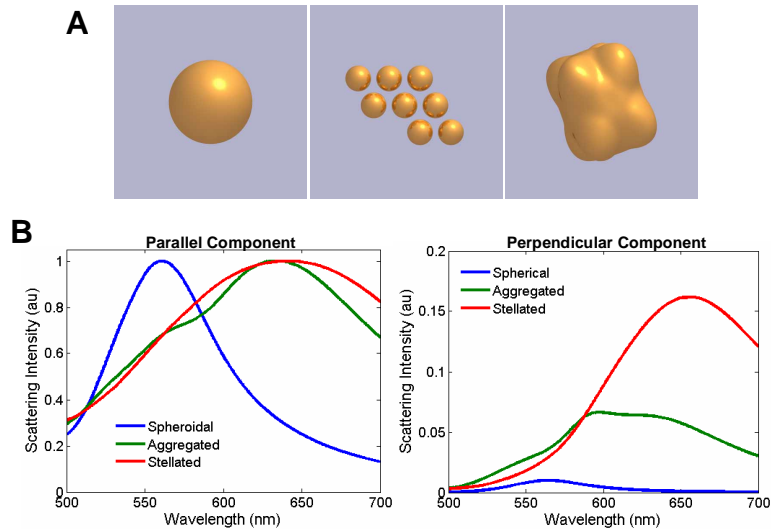

Fig. 3. (A) Computer-generated images showing the geometries that were used for electrodynamic simulations: a 75nm diameter, 1.05 aspect ratio spheroidal particle (left); an aggregate of 8 spherical particles with 65 nm diameter and a center-to center separation of 1.15 times the particle diameter (middle); and a stellated particle (right), which was designed to closely approximate particle number 2 shown in Fig. 1(b). In each case, incident illumination propagates in the z-direction (into the page). In (B), simulated scattering cross sections are shown for scattered polarization parallel (left) and perpendicular (right) to that of the incident light. Spheroidal particles and aggregates of spherical particles (blue and green curves, respectively) were simulated using a new implementation of T-Matrix theory, while stellated particles (red curves) were analyzed using publicly available discrete-dipole approximation (DDA) algorithms. Parallel spectra (B, left) are each normalized to a maximum of one. Spectra in (B), right, show the intensity of light scattering in the perpendicular direction relative to the normalized parallel scattering cross-section. Therefore, the perpendicular components (B, right) demonstrate the relative depolarization ability of each particle type/aggregate. Note that single stellated particles can depolarize up to *ca.* 15% of the incoming linear polarized illumination, while single spheroidal particles only depolarize *ca* 1%. The 8-particle aggregate depolarizes up to 7% of the incoming illumination.

These results demonstrate that for a material with no inherent birefringence properties such as gold, which has a face-centered-cubic (FCC) crystal lattice, symmetry considerations determine to what extent the scattered light retains the polarization of the incident light. For example, light scattered from a spheroidal particle depolarizes to a degree corresponding to the deviation of the particle's shape from a perfect sphere. Scattering from single particles with a complicated morphology such as stellated nanoparticles in many cases will also depolarize for analogous reasons. In addition, scattering from random aggregates of particles, almost regardless of the properties of the constituent particles, in general depolarizes. In this latter case, both symmetry and inter-object distance are important, as plasmon coupling between particles significantly enhances the depolarization effect.

3.1 Imaging EGFR assemblies in live cells using spherical and stellated nanoparticles

To test the use of stellated and spherical plasmonic nanoparticles as molecular specific, light depolarizing contrast agents, aliquots of A-431 keratinocyte cells (which express *ca.* 10^6 EGFRs/cell [59, 60]) were exposed to either anti-EGFR antibody-conjugated spherical or stellated particles for 30 minutes at room temperature under mild agitation. To evaluate the overall contrast enhancing potential of each type of particle, unlabeled A431 cells were mixed in a 1:1 ratio with labeled cells. This provides a mixture of labeled and unlabeled cells in a single field of view. Figure 4A shows darkfield images from the same field of view of a 1:1 mixture of unlabeled A431 cells and those labeled with anti-EGFR gold spheres (top row) and stellated nanoparticles (bottom row). Images show the color difference between the labeled cells which have orange and red patches and intrinsic blue scattering from unlabeled cells. It is well characterized that EGFR molecules form aggregates in protein-rich clathrin coated pits on the cell membrane [61]; this results in EGFR-mediated aggregation of gold nanoparticles and the red shift in the light scattering from the nanoparticles [11]. The blue scattering from unlabeled cells is apparent in images taken without polarizers (Fig. 4(a), left column), as well as images taken with polarizer/analyzer in parallel configuration (Fig. 4(a), middle column). In both cases, the overall signal intensity ratio between labeled and unlabeled cells is approximately 3. However, imaging the same field of view using perpendicular polarization, Fig. 4(a), right column, results in significant decrease in the scattering from unlabeled cells. This increases the signal ratio between labeled and unlabeled cells more than two-fold and nearly four-fold in the case of spherical and stellated nanoparticles, respectively. It is important to note that images with parallel and perpendicular orientation of polarizers were acquired under acquisition conditions with 14x and 30x increased sensitivity as compared to the image with no polarizers, respectively, to adjust for overall light throughput differences in each configuration, and to optimize the SNR in each image. To check for molecular specificity of anti-EGFR gold conjugates, EGFR negative MDA-MB-435 cells were exposed to anti-EGFR stellated particles. No labeling was observed, indicating a high degree of molecular specificity.

Hyperspectral measurements of labeled cells using the PARISS system were carried out in parallel with darkfield imaging to quantify polarization dependent spectral changes associated with EGFR-mediated clustering of the spherical and stellated nanoparticles (Fig. 4(b)). All spectra were averaged over the whole image of the cell, and were normalized to one at the maximum scattering wavelength. It can be seen that for cells labeled with either spherical or stellated particles, the relative contribution from scattering in the blue and green spectral regions is dramatically decreased when imaged in cross-polarization, relative to parallel orientation of polarizers; this decrease reveals plasmon resonance scattering from nanoparticle assemblies. This result correlates very well with the images in Fig. 4(a), which show a decrease in intrinsic blue scattering of cells. The hyperspectral imaging provides spectroscopic evidence that the scattering signal from closely spaced spherical or stellated nanoparticles can efficiently be distinguished from intrinsic cellular scattering by using polarization sensitive microscopy.

The spectra in Fig. 4(b) show that the maximum of the plasmon resonance scattering in both cases of aggregated particles (either spheroidal or stellated) is shifted significantly from that seen in isolated particles (compare with Fig. 1(e)). While isolated spherical nanoparticles have a peak scattering wavelength of approximately 560nm, this value is shifted to the red by 30-40nm when nanoparticles are bound to assemblies of EGFR molecules on the cell surface. Similarly, stellated nanoparticles display a large plasmon resonance shift in response to EGFR-mediated clustering, such that the scattering peak appears to lie outside the spectral range of the imaging system. This red shift was well characterized in the case of spherical particles and was attributed to plasmon coupling between closely spaced plasmonic particles[9-11, 40]. It is interesting to note that the same effect is displayed by stellated nanoparticles. This observation indicates that stellated nanoparticles may be used as "nano-rulers" similar to spherical nanoparticles[9]. Certainly, more monodisperse stellated particles,

as well as better understanding of stellated particle plasmon coupling are needed, before such an approach could be quantitatively implemented.
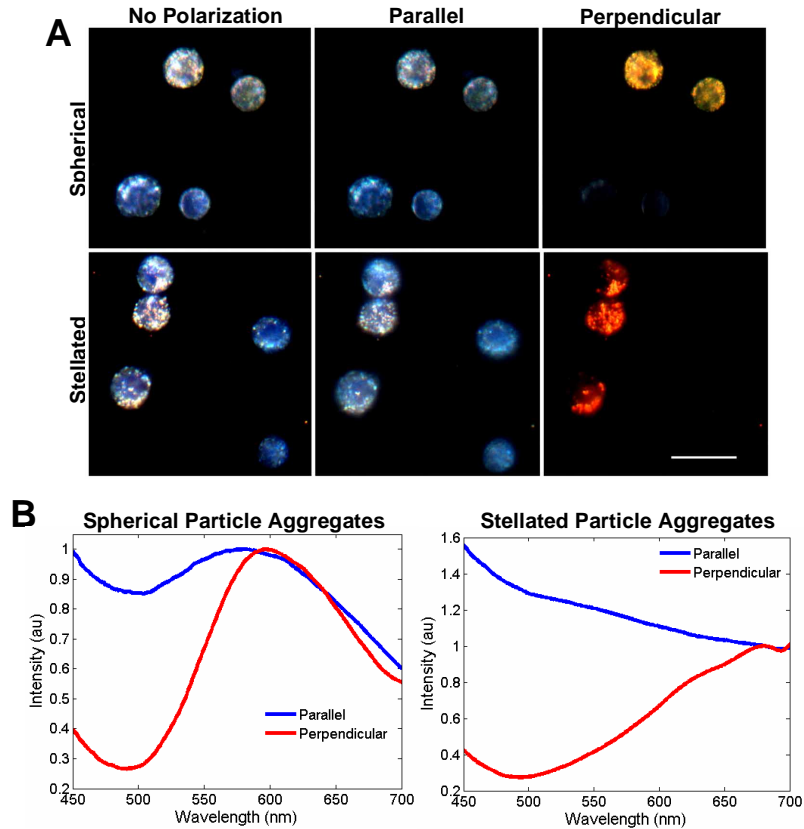

Fig. 4. Darkfield imaging and hyperspectral microscopy of live cells labeled with anti-EGFR spherical and with stellated gold nanoparticles. In (A), darkfield images of A431 cells labeled with spherical (top row) and stellated (bottom row) particles are shown. Labeled cells were mixed in a 1:1 ratio with unlabeled cells which appear blue due to intrinsic scattering from cells. Darkfield images of the labeled/unlabelled cell mixtures were obtained with no polarizers (left), and parallel (middle) and perpendicular (right) orientation of a linear polarized illumination and an analyzing polarizer. To optimize the SNR in each image, parallel and perpendicular images were acquired using acquisition conditions with 14x and 30x increased sensitivity, respectively, relative to non-polarized images. Imaging in cross-polarization resulted in a 3 to 4-fold increase in the signal ratio between labeled to unlabeled cells as compared to the parallel orientation. Therefore, unlabeled cells are not visible in the images shown for the cross-polarization (A, right). Scale bar is 20μm. Part (B) shows scattering spectra of cells labeled with spherical (left) and stellated (right) nanoparticles. The spectra were obtained in parallel (blue) and perpendicular (red) orientation of polarizers in illumination and detection paths using a PARISS hyperspectral imaging system (Lightform, Inc.) coupled to the Leica DM6000 microscope. The curves are normalized to one at the maximum of the cross-polarized (red) spectra to facilitate comparison of the spectral profiles. Note the large relative decrease in scattering in the blue spectral region when detection was carried out in cross-polarization mode, as well as a large red shift in scattering maximum of labeled cells as compared to isolated particles.

3.2. Imaging single EGFR proteins in live cells using stellated nanoparticles

Our results show that aggregated spherical and stellated nanoparticles depolarize light much more efficiently than cellular components. This effect can be used to increase molecular

specific signal in imaging of biomolecular assemblies. However, there is also great interest in monitoring single molecular events in living cells In this case, the use of stellated gold nanoparticles in combination with polarization microscopy offer significant advantage over spherical nanoparticle geometry because of the high depolarization efficiency of stellated nanoparticles (Figs. 1 and 2). We combined anti-EGFR stellated nanoparticles and polarization dark-field transmittance microscopy to demonstrate the possibility of single nanoparticle and, therefore, of a single molecule detection inside a live cell. To operate in the single molecule imaging regime, the probability of multiple particles existing in the same imaging voxel must be sufficiently reduced. To accomplish this, stellated nanoparticles were diluted 5-fold relative to the original concentration.   This corresponds to an absolute concentration of *ca.* 10^9 particles per mL, or an average particle-to-particle separation distance of 10µm in solution which is well beyond the sub-micron lateral resolution of the microscope with a 40x objective. Therefore, having two particles in the same pixel at the same time is highly unlikely. In addition, we utilized SiHa cervical cancer cells, which express *ca.* 10^4-10^5 EGFR molecules per cell[62], or 10-100-fold fewer than the A431 cells shown in Fig. 4. SiHa cells were cultured as described in the Materials and Methods section on glass coverslips. Then coverslips with live SiHa cells were placed on top of a microscope slide with a 100µm-thick chamber containing diluted anti-EGFR stellated nanoparticles. We observed an extremely low labeling density in cells (0-2 particles per cell) at this nanoparticle concentration, and this also indicates a very low likelihood of having more than one nanoparticle in the same imaging pixel. Live cells were imaged using the Leica DM6000 microscope with polarizer and analyzer axes positioned perpendicular to each other. Color images were acquired at 10 second intervals in cross-polarization mode for 60 minutes. Phase contrast images without polarizers were acquired in order to reveal the cellular position and morphology. The time-course tracking of single EGFR-bound stellated particle is shown as a movie in Fig. 5.
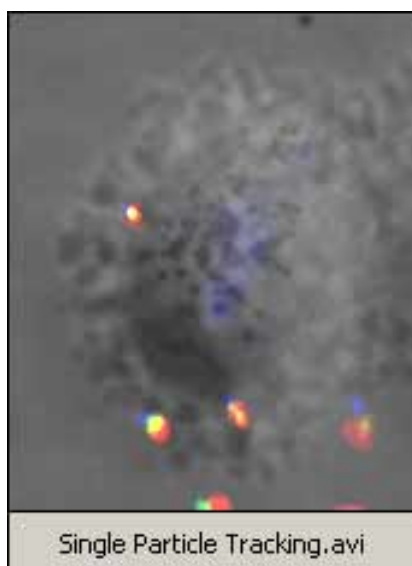

Fig. 5. Video clip showing movement of individual stellated nanoparticles bound to EGFR molecules in live SiHa cells. Note the presence of unbound particles moving quickly through the field of view. Bound particles show slower, directional movement towards the cell nucleus, consistent with receptor-mediated endocytosis.

Serially acquired darkfield images are overlaid with a phase contrast image of the same field of view to indicate the relative position of individual particles in the cell. In this movie, unbound particles quickly move through the field of view while EGFR bound nanoparticles

undergo much slower directional motion within the cell toward the nucleus. Analysis of darkfield images indicates that the signal to background ratio between single stellated particles and the intrinsic cell scattering is approximately 6. Dark-field and phase contrast images taken from the movie shown in Fig. 5 are overlaid in Fig. 6 at two different time points. Fig. 6(b) shows the particle locations approximately 10 minutes after acquisition of the image shown in Fig. 6(a) with traces of the lateral path that each particle took during the intervening time between each image capture. This demonstrates the possibility of tracking of individual particles bound to an EGFR molecule in live cells with high signal-to-background ratio. The observed trafficking of the nanoparticles toward the center of the cell (Figs. 6(a) and 6(b)) is consistent with the current models of EGFR regulation based on endocytosis and subsequent movement into the perinuclear region of the cell [63]. In addition, the intensity of the scattering signal from the nanoparticles shown in Figs. 6(a) and 6(b) correlates well with the average intensity of single stellated nanoparticles shown in Fig. 1. In order to provide additional evidence that the signal in Figs. 6(a) and 6(b) is associated with *single* particles, hyperspectral imaging was carried out on the same sample. Figure 6(c) shows a spectrum that was acquired from one of the EGFR bound particles, as noted by the arrow. The scattering spectrum has a peak at approximately 620nm, which is in good agreement with spectra acquired from individual particles (see Fig. 2).
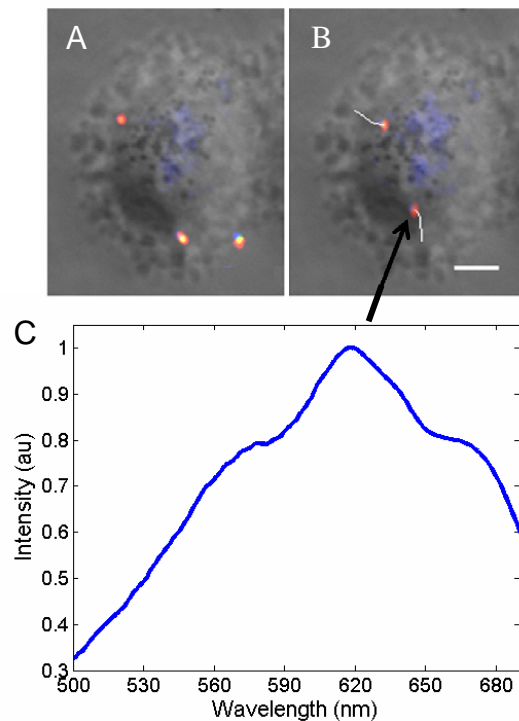

Fig. 6. Imaging of single stellated particle trafficking inside live SiHa cells. Single particles bound to EGFR molecules on SiHa cells were imaged at 10 second intervals under cross-polarized, transmitted darkfield mode. These images were overlaid with a phase contrast image taken of the same field of view. There is 10 minute interval between images shown in (A) and (B). White lines indicate trafficking paths of single stellated nanoparticles which are attached to EGFR molecules within the live SiHa cell. Note an unbound particle in (A) which quickly moves from the field of view and is therefore not present in (B). Scale bar is 5µm. Scattering spectrum of an EGFR-bound particle (indicated by an arrow) is shown in (C). The spectrum was acquired using the PARISS hyperspectral imaging system coupled to the Leica DM6000. The plasmon resonance wavelength of this particle is consistent with the spectral profile measured for isolated stellated particles (see Fig. 2).

In addition, the spectral line width (FWHM) of the particle shown in Fig. 6 is *ca.* 159nm, which is statistically identical to the estimated mean of 153±32nm found for a population of individual particles. The spectral analysis provides additional evidence for the tracking of single nanoparticles in images shown in Fig. 6.

4. Conclusions

Due to the stochastic nature of living cells, the characterization of their behavior at the single molecule level is a much sought-after capability [64]. Such an approach can result in a more informative elucidation of protein regulatory and signaling pathways that otherwise may be difficult or impossible to unravel via bulk measurements. Optical imaging with plasmonic nanoparticles has the potential to provide a way to monitor these single events dynamically, with high molecular specificity over long periods of time. Addition of intra-cellular delivery peptides to the particle surface as was recently described in [23,77] may allow the monitoring of cytoplasmic proteins in live cells. In this manuscript we have described a combination of a new type of plasmonic nanomaterial – stellated nanoparticles – and a simple polarization sensitive detection scheme that can be used for sensitive detection of molecular assemblies and single molecular events such as EGFR activation and trafficking inside live cells. Our approach takes advantage of strong depolarization of linear polarized excitation light by stellated nanoparticles. High signal-to-background ratio (SBR) is possible in this case without the use of methods that restrict the signal collection volume, such as confocal microscopy [65], fluorescence correlation microscopy [66], or total internal reflection fluorescence (TIRF) imaging [67] which are necessary in fluorescence based single molecule studies (see examples in [1, 2, 68-70]). We envision that incorporating any these methods to image molecular specific stellated gold nanoparticles in living cells would significantly increase the SBR beyond what is reported here.

The combination of plasmonic nanoparticles with polarized illumination and polarization sensitive detection schemes presented here can be potentially extended to *in vivo* applications. Photon scattering within cellular tissues typically takes several interaction events before polarization is randomized that can occur over length scales in the order of the hundreds of microns for optically transparent tissues such as epithelium [71]. This phenomenon is the basis for spectroscopic techniques that can distinguish between optical signals from superficial epithelial tissues and deeper connective layers [41, 72-74]. Polarization sensitive approaches are also applied in high resolution endoscopic methods including confocal reflectance microscopy [75] and optical coherence tomography [76]. These methods can be easily adapted for polarized imaging and spectroscopy of plasmonic nanoparticles *in-vivo*. Therefore, strong light depolarization by plasmonic nanoparticles and their assemblies can afford molecular specific imaging with improved signal-to-background ratio in the epithelium tissue for applications such as early cancer detection.